

Thesis Title

A subtitle of your thesis

Author name



Thesis submitted for the degree of
Master in Master's Program Name <change at
main.tex>
60 credits

Department Name <change at main.tex>
Faculty name <change in duoforside.tex>

UNIVERSITY OF OSLO

Spring 2022

Thesis Title

A subtitle of your thesis

Author name

© 2022 Author name

Thesis Title

<http://www.duo.uio.no/>

Printed: Reprosentralen, University of Oslo

Abstract

Contents

1	Introduction	1
I	Theory	3
2	High-Entropy alloys	4
2.1	Fundamentals	4
2.2	Core effects and properties	7
3	Modeling of random alloys	9
3.1	The Special Quasi-random Structure model	9
3.1.1	Mathematical description	10
3.1.2	Applications to high-entropy alloys	12
4	Density Functional Theory	16
4.1	Review of Quantum Mechanics	17
4.1.1	The Shrödinger equation	17
4.1.2	Approximations to the many-body Shrödinger equation	18
4.2	Kohn-Sham density functional theory	20
4.2.1	Density functional theory	20
4.2.2	The Kohn-Sham Equation	21
4.3	Limitations of DFT	22
II	Method	24
5	Practical aspects of DFT	25
5.1	The Exchange-Correlation functional	25
5.1.1	Local density approximation	25
5.1.2	Generalized gradient approximation	26
5.1.3	Meta-GGA	26
5.1.4	Hybrid functionals	27
5.1.5	Outlook	27
5.2	Plane waves and reciprocal space	28
5.3	Self-consistent field calculation	30

6	Computational details	32
6.1	Settings and dependencies	32
6.2	Material	33
III	Results and Discussion	35
7	The high-entropy silicide (CrFeMnNi)Si₂	36
7.1	Bulk β -FeSi ₂	36
7.2	(CrFeMnNi)Si ₂ SQSs	37
7.2.1	The band gap	39
7.2.2	Local and projected density of states	43
7.2.3	The band gap with SCAN and HSE06	45
7.2.4	Pair distribution functions	50
7.2.5	SQS size	52
8	Other compositions	56
8.1	Exploring the quaternary phase-diagram	56
8.2	High entropy silicides with cobalt and titanium	60
IV	Conclusion	67
10	Overview and outlook	65
10.1	Literature	65
10.2	General thoughts	66
10.3	Other things	70
10.4	Cr ₄ Fe ₄ Mn ₄ Ni ₄ Si ₃₂ in different crystal structures	73
10.5	Overview	75
A	Compositions	66
A.1	Projected density of states	66
A.2	Probability distribution functions	69
B	Eqvimolar alloy	71
B.1	DOS	71
C	Charge density	80

List of Figures

2.1	Formation of HEA based on δ and N . Figures adopted from [hea2016_ch2]	6
2.2	A schematic illustration of lattice distortion in high-entropy alloys. Figure from [owen_jones_2018]	8
3.1	PDFs of (a) 20 and (b) 250 atom SQS models of CrFeMnNi [hea2016_ch10]	13
3.2	Density of states with SQS and MC/MD of FCC CoCrFeNi, figure from [hea2016_ch10]	14
3.3	Probability distribution functions with SQS and MC/MD of HCP CoOsReRu [hea2016_ch10]	14
4.1	Number of DFT studies per year from 1980 to 2021 [dimensions].	16
5.1	Calculated to experimental band gap measurements of Becke-Johnsoon, modified Becke-Johnson and SCAN functionals [xc_benchmark]	27
5.2	Self consistent iteration of a DFT calculation. Figure adopted from lecture notes fys-mena4111 [persson2020]	30
6.1	5 distinct 48 atom SQS of $\text{Cr}_4\text{Fe}_4\text{Mn}_4\text{Ni}_4\text{Si}_{32}$ based on the β -FeSi ₂ crystal structure. Illustrated with VESTA [vesta]	33
7.1	Density of states (PBE) β -FeSi ₂	37
7.2	Density of states of SQS D (CrFeMnNi)Si ₂ with PBE.	39
7.3	Density of states of SQS B (CrFeMnNi)Si ₂ with PBE.	39
7.4	Local density of states of Si (SQS D)	43
7.5	Local density of states of (a) Cr, (b) Mn, (c) Fe, (d) Ni in SQS D.	43
7.6	Projected density of states SQS D CFMN (fesi2) from PBE calculation	44
7.7	Projected density of states of SQS D and B around E_F	44
7.8	Density of states illustrating the band gaps from PBE and SCAN calculations for SQS E and D.	46
7.9	Density of states of SQS B with HSE06	46
7.10	Pair distribution functions of SQS D (top) and B (bottom)	50
7.11	CPU time of 48, 96 and 192-atom SQSs of (CrFeMnNi)Si ₂	52
7.12	Density of states of SQS E 192 atom SQS.	54

7.13	Pair distribution functions of SQS sizes (top) 48 atoms, (middle) 96 atoms, (bottom) 192 atoms	55
8.1	Projected density of states of (a) $\text{Cr}_3\text{Fe}_3\text{Mn}_7\text{Ni}_3\text{Si}_{32}$ (SQS B), (b) $\text{Cr}_5\text{Fe}_5\text{Mn}_3\text{Ni}_3\text{Si}_{32}$ (SQS C), (c) $\text{Cr}_5\text{Fe}_3\text{Mn}_5\text{Ni}_3\text{Si}_{32}$ (SQS A), (d) $\text{Cr}_3\text{Fe}_5\text{Mn}_5\text{Ni}_3\text{Si}_{32}$ (SQS D)	59
8.2	Projected density of states of $\text{Cr}_3\text{Fe}_3\text{Mn}_3\text{Ni}_7\text{Si}_{32}$ around E_F .	59
8.3	Projected density of states of $(\text{CrFeMnCo})\text{Si}_2$	63
8.4	Density of states of a) $(\text{CrFeCoNi})\text{Si}_2$ and b) $(\text{CrFeTiNi})\text{Si}_2$. .	64
8.5	Density of states of two lesser stable SQSs of $(\text{CoFeMnNi})\text{Si}_2$. .	64
A.1	$\text{chCr}_4\text{Fe}_4\text{Co}_4\text{Ni}_4\text{Si}_{32}$	66
A.2	$\text{chCo}_4\text{Fe}_4\text{Mn}_4\text{Ni}_4\text{Si}_{32}$	67
A.3	$\text{chCr}_4\text{Fe}_4\text{Mn}_4\text{Co}_4\text{Si}_{32}$	67
A.4	$\text{chCr}_4\text{Fe}_4\text{Ti}_4\text{Ni}_4\text{Si}_{32}$	68
A.5	$\text{chCr}_4\text{Fe}_4\text{Mn}_4\text{Ti}_4\text{Si}_{32}$	68
A.6	Probability distribution functions of top: $\text{Co}_4\text{Fe}_4\text{Mn}_4\text{Ni}_4\text{Si}_{32}$ (SQS D), middle: $\text{Cr}_4\text{Fe}_4\text{Co}_4\text{Ni}_4\text{Si}_{32}$ (SQS B), bottom: $\text{Cr}_4\text{Fe}_4\text{Mn}_4\text{Co}_4\text{Si}_{32}$ (SQS B)	69
A.7	Probability distribution function of top: $\text{Cr}_4\text{Fe}_4\text{Mn}_4\text{Ti}_4\text{Si}_{32}$ (SQS B), bottom: $\text{Cr}_4\text{Fe}_4\text{Ti}_4\text{Ni}_4\text{Si}_{32}$ (SQS B))	70
B.1	Density of states SQS A $(\text{CrFeMnNi})\text{Si}_2$ with PBE.	71
B.2	Density of states SQS E $(\text{CrFeMnNi})\text{Si}_2$ with PBE.	72

List of Tables

7.1	Total energy per atom, final magnetic moment and band gap of 5 unique SQS of (CrFeMnNi)Si ₂ based on the β -FeSi ₂ unit cell.	37
7.2	Band gap of the 5 SQSs of (CrFeMnNi)Si ₂ calculated from the eigenvalues in spin up, down and total.	40
7.3	Band gap of SQS D as a function of occupancy in the eigenvalues.	41
7.4	Band gap calculated with PBE, SCAN and HSE06 XC-functionals of (CrFeMnNi)Si ₂ SQSs.	45
7.5	Minimum gap between k-point in valence band and conduction band in SQS B from PBE, SCAN and HSE06	47
7.6	Band gap from HSE06 calculations with Gaussian smearing and smearing width <i>sigma</i> equal to 0.05 and 0.005, and the tetrahedron method (TBC). "-" means unchanged	48
7.7	Total energy, magnetic moment and formation energy of 48, 96 and 192 atom SQSs of (CrFeMnNi)Si ₂	52
7.8	Band gap of SQSs of 48, 96 and 192-atoms of (CrFeMnNi)Si ₂ . The names are arbitrary, ie A in 48 does not equal A in 96 or A in 192. The values listed in <i>cursive</i> indicate a defect band gap.	53
8.1	Summary composition diagram	56
8.2	Band gaps of various compositions of (CrFeMnNi)Si ₂ . Most stable SQS of a set is highlighted in bold text, defect band gap are listed in cursive. Some SQSs were excluded from the table due to unsuccessful calculations.	58
8.3	Overview new compositions	61
8.4	Final magnetic moment of the most stable supercell of each composition.	62
8.5	Band gaps of the most stable SQS of β -FeSi ₂ high-entropy silicide compositions as a function of occupancy in the eigenvalues.	62
10.1	Mean and stadard deviation of the total energy and magnetic moment per atom, plus enthalpy of formation of the listed mean energies (FeSi ₂).	68

10.2 Total and spin dependent band gap of 4 permutations of CFMN (fesi2) with PBE GGA calculation. The structures that are excluded from this list either failed in calculations, or does not show any band gap.<	70
---	----

Preface

Gotta give a shout out for my mans Jens

Chapter 1

Introduction

some introduction on the importance of discovering new materials and alloying.

Need something on thermoelectricity related to both the band gap and high-entropy alloys.

High-entropy alloys is a novel class of materials based on alloying multiple components, as opposed to the more traditional binary alloys. This results in an unprecedented opportunity for discovery of new materials with a superior degree of tuning for specific properties and applications. Recent research on high-entropy alloys have resulted in materials with exceedingly strong mechanical properties such as strength, corrosion and temperature resistance, etc **find references**. Meanwhile, the functional properties of high-entropy alloys is vastly unexplored. In this study, we attempt to broaden the knowledge of this field, the precise formulation of this thesis would be an exploration on the possibilities of semiconducting high-entropy alloys.

A key motivation of this thesis is the ability to perform such a broad study of complex materials in light of the advances in material informatics and computational methods. In this project, we will employ Ab initio methods backed by density functional theory on top-of the line supercomputers and software. 20 years ago, at the breaking point of these methods, this study would have been significantly narrower and less detailed firstly, but secondly would have totaled ... amount of CPU hours to complete (**Calculate this number**). In the addition to the development in computational power, is also the progress of modeling materials, specifically we will apply a method called Special Quasi-random Structures (SQS) to model high-entropy alloys or generally computationally complex structures. Together with the open landscape of high-entropy alloys described above, these factors produce a relevant study in the direction of applying modern computational methods to progress the research of a novel material class and point to promising directions for future research.

In specifics, this thesis revolve around the electrical properties of high-entropy alloys, mainly the band gap as this is the key indicator for a semiconducting material and it's applicability. Semiconductors are the building blocks in many different applications in today's world, ranging

from optical and electrical devices, to renewable energy sources such as solar and thermoelectricity. Given the economic and sustainable factors concerning silicon, in addition to its role in relevant applications such as microelectronics and solar power. Silicon emerges as a natural selection to build our alloys around. Furthermore, the development and research on both high entropy alloys and metal silicides have been heavily centered around 3d transition metals. Keeping in line with the economic and environmental factors, we will continue this direction by focusing on high entropy stabilized sustainable and economic 3d metal silicides **Not happy with this writing**. Throughout the study we will analyze a great number of permutations of 3d silicides, from different initial metal silicides such as $CrSi_2$, $FeSi_2$, $MnSi_{1.75}$, Fe_2Si , each with distinct properties relating to the band gap, crystal structure and metal to silicon ratio. In addition, the permutations include numerous metal distributions and elements within the 3d-group of metals. Examples are Co, Cr, Fe, Mn, and Ni.

Given a background in high-entropy alloys, one could ask if this study is truly sensible. In the later sections we will cover the details of this field, and it quickly become clear that the materials investigated in this study does not fall under the precise definition of high-entropy alloys, nor do we intend to explore the properties and factors relating to high-entropy stabilized alloys such as the configurational entropy, phase stability and finite temperature studies. However this study is motivated from the discovery of these materials and promising properties, and venture into a more hypothetical space of materials, enabled by the computational methods available to study the potential properties of such materials. On the other hand, very recent studies **Mari, and other HEA silicide study** have experimentally synthesized high-entropy disilicides, thus in some way justifying the direction of this project.

We begin this project by reviewing key concepts of solid-state physics for readers lacking a background in materials science, and an introduction to the base 3d silicides of the experimental work. Later follows a theoretic walk-through of the relevant concepts of this thesis, these topics include high-entropy alloys, special quasi-random structures, and density functional theory. Next we shine light on the implementation of DFT in this project, and other computational details required to reproduce the results in this thesis, such as the use of the Vienna Ab Initio Simulation Package (VASP) and implementation of SQS. Finally we present the results of our study, these include the band gap and electronic properties of various structures and the success and challenges of the computational methods applied throughout the study.

Part I

Theory

Part II

Method

Part III

Results and Discussion

Chapter 7

The high-entropy silicide (CrFeMnNi)Si₂

7.1 Bulk β -FeSi₂

We begin by presenting a brief overview of the parent compound β -FeSi₂ that we have used as a foundation in this project.. In addition this is the sole case in this project where our methods and results can be compared to experimental work and relevant literature.

β -FeSi₂ is a well known semiconductor with an experimentally measured band gap of around 0.85 eV at room temperature [1]. The nature of the band gap is under debate, all though most ab initio studies result in an indirect gap, experimental studies agree on a direct band gap. From our own calculations we get an indirect band gap of 0.65 eV with PBE GGA functional. In comparison materials project list a band gap of 0.70 eV with the same functional. This slight discrepancy is most likely down to use of different parameters in the calculations, for example the cutoff energy or number of k-points. In agreement with materials project our calculations return a final magnetic moment of the compound equal to 0, this can be seen in the electronic density of states of the material plotted in figure 7.1, by that the DOS and hence band gap is identical in both spins.

The formation energy E_{form} of the compound can be calculated as the difference in total energy between the product and the sum of reactants. For the FeSi₂ compound that consist of 16 iron atoms and 32 silicon we get

$$E_{\text{form}} = -327.72\text{eV} - (16 \times -8.32\text{eV} + 32 \times -5.42\text{eV}) = -21.16\text{eV},$$

or formation energy per atom $E_{\text{FPA}} = 0.441\text{eV}$ from $-21.16/48$. The total energy of iron and silicon was calculated separately for the respective base elements with identical parameters as used for the FeSi₂ calculation. The total energies correspond well with the listed energies from materials project of -8.4693 eV and -5.4234 eV for Fe and Si respectively. Accordingly the formation energy per atom for β -FeSi₂ of 0.441 eV is in good agreement with materials project's value of 0.444 eV for β -. Again, the

difference is most likely related to materials project utilizing a larger energy cutoff of 520 eV compared to our value of 300 eV.

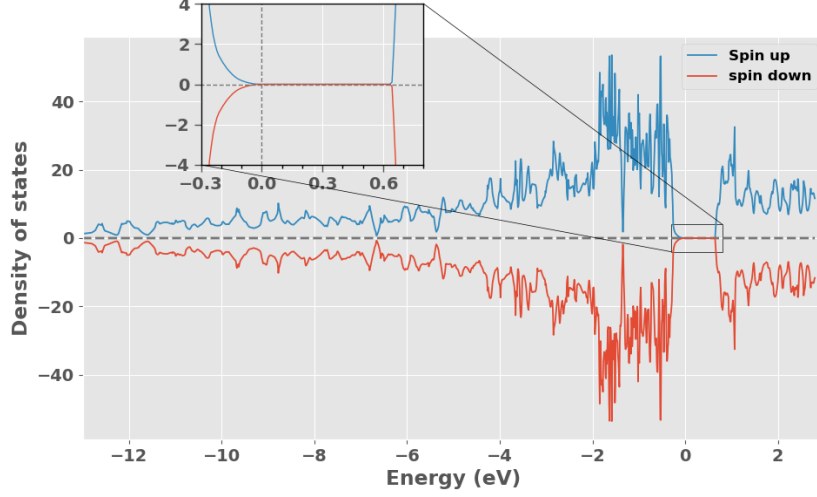


Figure 7.1: Density of states (PBE) β -FeSi₂

7.2 (CrFeMnNi)Si₂ SQSs

Below in table 7.1 we list the total energy per atom (Toten), final magnetic moment per atom (Mag) and band gap (E_G) of five unique SQSs of the Cr₄Fe₄Mn₄Ni₄Si₃₂ alloys based on the β -FeSi₂ structure. In addition we include the mean and standard deviation (std) between the 5 supercells and the formation energy calculated from the mean total energy. Details on the generation and general features of the alloys is provided in section 6.2.

SQS	Toten (eV)	Mag (μ_B)	E_G (eV)
A	-6,6080	0.0833	0.0280
B	-6,6138	0.0833	0.0523
C	-6,6063	0.0834	0.0344
D	-6,6155	0.0833	0
E	-6,6089	0.0833	0.0495
Mean	-6.6105	0.0833	0.0328
Std	0.0039	0.0000	0.0210
$E_{FPA}(eV)$	-0.293	-	-

Table 7.1: Total energy per atom, final magnetic moment and band gap of 5 unique SQS of (CrFeMnNi)Si₂ based on the β -FeSi₂ unit cell.

From table 7.1 we observe that the total energy and magnetic moment are quite similar in all 5 supercells, which could be expected from that the atomic configuration is the only variable. On the other hand the atomic

configuration have a larger impact on the band gap of the supercells. We find that the band gap ranges from a maximum value of 0.05 eV in SQS B, to a metal in SQS D, nevertheless much smaller than FeSi₂ (0.65 eV). We will come back to discussing the band gaps in later sections.

Compared to the bulk material we find that the alloy apparent from all five supercells display a finite magnetic moment of around $0.083\mu_B$. The local magnetic moments show some variation between supercells but follow the same trend where the largest moments are attributed to chromium atoms in the lattice, followed by manganese. On the other side the magnetic moments of both iron and nickel within the numerical accuracy of the calculations give negligible contributions to the magnetic moment of the structures. Considering that the total magnetic moment is identical in 5 distinct atomic configurations and the local magnetic moments show very similar trends, the observed magnetism within the scope of this project is most probably connected to the particular crystal structure. It should be noted however that the magnetic properties in this project could be prone to errors. As we discussed in section 4.3 one of the major drawbacks of DFT in regards to magnetic materials is the local minima problem. In this project we have overlooked this concern and applied a constant initial co-linear magnetic configuration in all structures in order to reduce the workload, thus it's possible that the final magnetic structure of the supercells adopt local minimas rather than global. Coupling this with the possible errors associated with the special quasi-random structures method to model the disordered magnetic structure means that the magnetic results and following the total energy and corresponding stability are not immutable nor necessarily accurate in respect to the hypothetical real alloy.

In terms of the total energy the most and least stable SQSs are "D" and "A" respectively, meaning that SQS D is then the most representative configuration of the real material. However most likely all five SQSs and other possible configurations would appear as local orderings in domains of the real material with a certain probability. Therefore we will consider and discuss the results of all 5 SQSs as well as the most stable supercell. Further the total energy alone is not sufficient to evaluate the stability of the structure. In this project we have not considered factors such as the configurational entropy or made any finite temperature considerations in general. Additionally the discussion above on the magnetic configuration could affect the total energy. Thus the relative stability between supercells listed in table 7.1 could be variable, nevertheless the most stable configuration is moderately emphasized from the considerations made in this project.

7.2.1 The band gap

As seen from table 7.1 the band gap of the alloy are severely reduced from the bulk material, and vary from supercell to supercell. We observed a maximum band gap of 0.05 eV in SQS B, and on the flip side a 0 band gap in the utmost stable configuration SQS D. The density of states of SQS D and B is displayed in figures 7.2 and 7.3 below, similar plots can be found in appendix [REF] for the other supercells.

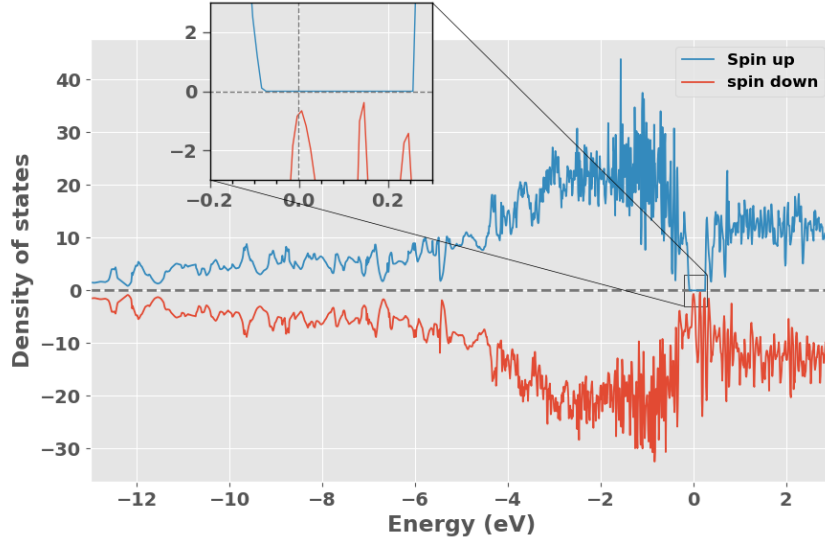


Figure 7.2: Density of states of SQS D (CrFeMnNi)Si₂ with PBE.

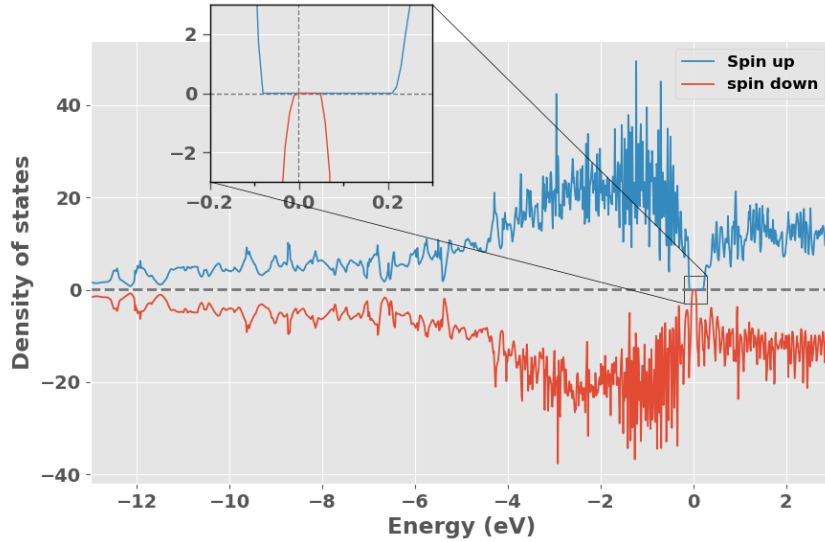


Figure 7.3: Density of states of SQS B (CrFeMnNi)Si₂ with PBE.

In figure 7.2 and 7.3 we observe that the band gap in both SQS D and B

in accordance with the magnetic property is different between spins. Going forward we will refer to the band gap in spin up as E_G^{up} , and spin down as E_G^{dw} . Clearly in both D and B $E_G^{\text{up}} \gg E_G^{\text{dw}}$ as SQS D for instance exhibits a band gap of around 0.3 eV in spin up, contrary to a 0 band gap in spin down. Comparing to the values in table 7.1 we find that the total band gaps of the respective structures is limited by the narrow or nonexistent band gap in spin down. To obtain further and more precise information on the band gap we look to the calculated Kohn-Sham eigenvalues. The eigenvalue band gaps, denoted as E_G^{eigen} can be seen below in table 7.2 for all five SQS, where the utmost stable configuration (SQS D) is highlighted in bold text. Continuing the trend described above we observe equivalent to SQS D and B that $E_G^{\text{up}} \gg E_G^{\text{dw}}$ for all supercells, par SQS A where the spin polarization of the band gap is less prominent and the total band gap is the combined sum of E_G^{up} and E_G^{dw} .

SQS	$E_G^{\text{up, eigen}}$ (meV)	$E_G^{\text{dw, eigen}}$ (meV)	$E_G^{\text{tot, eigen}}$ (meV)
A	81.4	52.2	28.1
B	293	52.2	52.2
C	236	34.3	34.3
D	339	0.00	0.00
E	308	50.0	50.0

Table 7.2: Band gap of the 5 SQSs of (CrFeMnNi)Si₂ calculated from the eigenvalues in spin up, down and total.

In VASP the energy eigenvalues are listed for every energy band at all k-points used in the calculation, with corresponding occupancy. An occupancy of 1 represents a fully occupied eigenstate, in analog a completely unoccupied (empty) eigenstate have occupancy equal to 0. Recalling that occupied states belong to the valence band, and the conduction band consists of unoccupied states (at 0 K). The highest energy valence band in these structures are band 124 in spin down and 128 in spin up, following the lowest energy valence band is 125/129 in spin down/up. The band gap in spin down is then determined from the difference between the lowest energy eigenvalue in band 125 and the highest energy eigenvalue in band 124, and likewise for the spin up band gap between bands 128 and 129. In SQS D different from the semiconducting structures we observe some partially occupied states at the band edges in bands 124 and 125 in spin down. With partially occupied states we refer to eigenstates in the valence band with occupancy less than 1 and states in the conduction band with occupancy above 0. Specifically the highest energy eigenvalue (9.01 eV) in band 124 have occupancy equal to 0.94, and equivalently the lowest energy eigenvalue (8.98 eV) in band 125 have occupancy equal to 0.08. This results in a 0 (negative) band gap. Further the Fermi energy in this structure is 8.99 eV, the partially occupied eigenstate in band 124 is then above the Fermi energy, and the partially unoccupied eigenstate in

the conduction band below the Fermi energy. This is a clear indication of a metal, in which the conduction band and valence band overlap. In this project we will refer to such eigenstates with partial occupancy as defect states. The importance of the defect states on the band gap in SQS D can be seen clearly in table 7.3. Here we calculate the band gap as a function of the defect states by an occupancy parameter occ , such that $E_G(0.99, 0.01)$ is the band gap when only including eigenvalues with corresponding occupancy above 0.99 in the valence band and below 0.01 in the conduction band. For simplicity we will write the parameter as a single value, where $occ = 0.01$ represents occupancy equal to 1 - 0.01 in the valence band and 0 + 0.01 in the conduction band.

occ	$E_G^{\text{up, eigen}}$ (meV)	$E_G^{\text{dw, eigen}}$ (meV)	$E_G^{\text{tot, eigen}}$ (meV)
0.5	339	0	0
0.05	339	21.0	21.0
0.01	339	49.6	49.6
0.001	339	73.3	73.3
<0.0001	339	85.7	85.7

Table 7.3: Band gap of SQS D as a function of occupancy in the eigenvalues.

From table 7.3 we find clear evidence of the defect states prohibiting the band gap in spin down in SQS D, compared to the semiconducting supercells that contain only fully occupied and unoccupied eigenstates. To investigate this effect to greater extent we compare the eigenvalues of SQS D to a pure metal, such as iron. In this case the energy bands (both spins) around the Fermi energy (5.8 eV) is populated mostly by partially filled eigenstates. Inside a single energy band we observe instances of both more than half-filled states above E_F , and less than half-filled states above E_F , thus clearly overlap between the conduction and valence band. In contrast we find no instances of partial occupants in pure Si, as in the semiconducting SQSs. Therefore we can firmly state that the "defect states" are associated with a metallic character. Compared to the pure metal however, the amount and severity of the partial occupants are very dampened in SQS D. The concept of defect or impurity states in the band gap have been found as a common feature of the band structure of random alloys [2], however we have reservations about if this is a physical result or related to numerical factors. In addition to partial occupants in Fe and SQS D we observe a plural of non-naturalistic states where the occupancy exceeds 1 and 0. Recalling that the discontinues Fermi surface of metals poses several obstacles on DFT calculations with respect to the smearing and number of k-points. This result could then be imagined as a consequence of numerical methods. For instance in SQS B we conducted three separate electronic calculations, one with the tetrahedron method (value listed in tables) and two calculations with Gaussian smearing with smearing width 0.05 and 0.005 eV. With the Gaussian method and smearing

width $\sigma = 0.05\text{eV}$ we get $E_G^{\text{up, eigen}} = 0.2987\text{eV}$ and $E_G^{\text{dw, eigen}} = 0.0497\text{eV}$. Further calculations with the Gaussian method with smearing width of 0.005 eV results in $E_G^{\text{up, eigen}} = 0.2932\text{eV}$ and $E_G^{\text{dw, eigen}} = 0.0522\text{eV}$. Compared to the values in table 7.3 with TBC, we observe that Gaussian (0.005 eV) and TBC are identical, while Gaussian (0.05 eV) show some deviation. Furthermore we find that the eigenvalues of Gaussian 0.05 eV contain defect states, and that the spin down band gap can thus be enlarged as in SQS D previously by $E_G^{\text{dw, eigen}}(0.01) = 0.1695\text{eV}$. However, in this case we find no instances of non-naturalistic states as we described above for SQS D with TBC.

In conclusion, the defect states observed in SQS D is clearly related to metallic properties, however from the discussion above we have seen that the results could be subjected to numerical factors as well. It would have been instructive to visualize and analyze the eigenvalues by plotting the band structure. Unfortunately this is neither simple to perform or interpret in large supercells consisting of several elements and a large number of energy bands. One solution to this is to perform band-unfolding, but this did not work in conjunction with the TDEP implementation of the special quasi-random structures method.

7.2.2 Local and projected density of states

In this section we will analyze the local and projected density of states of primarily SQS D (most stable). Below we include the local density of states of silicon in figure 7.4, and the respective LDOS plots of the various 3d elements of the compound in figure 7.5.

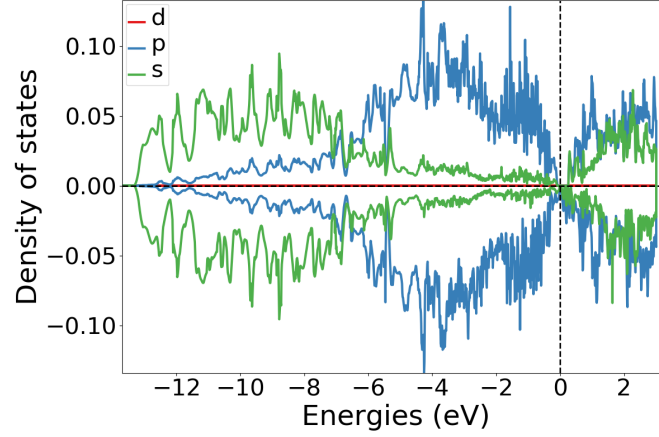


Figure 7.4: Local density of states of Si (SQS D)

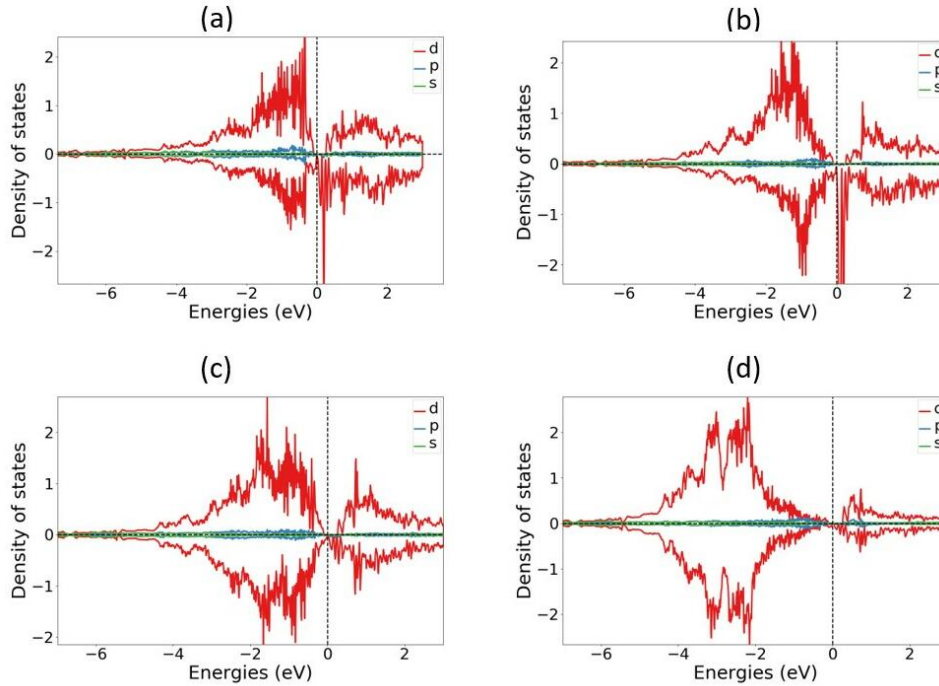


Figure 7.5: Local density of states of (a) Cr, (b) Mn, (c) Fe, (d) Ni in SQS D.

In the local density of states plotted in figure 7.4 we see that the s-electrons in Si occupy states in the lower energy regions and p electrons at slightly elevated energies closer to the Fermi energy. Above E_F states

are occupied by s and p electrons equally. Between the 3d electrons of the transition metals, markedly manganese and chromium display a strong presence at energies just above E_F and manganese additionally below E_F . Iron and Nickel show largest contributions at energies further from the Fermi energy, most notably below E_F . In the spin up channel we see a similar trend where chromium lies closest to E_F followed by manganese, iron and lastly nickel at the lowest energies. It could also be noted that in relation to the local magnetic moments discussed previously, we observe that the local density of states is symmetric with respect to spin in Fe and Ni, but not in Cr and Mn.

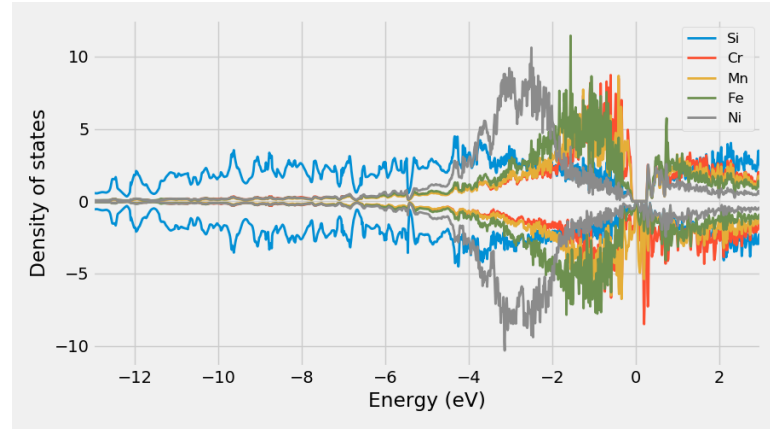


Figure 7.6: Projected density of states SQS D CFMN (fesi2) from PBE calculation

The interplay between 3d elements and silicon as shown in the projected density of states (figure 7.6) is in good agreement with observed trends in simpler Si-rich transition metal silicides [3] and Fe and Si β -FeSi₂ [4].

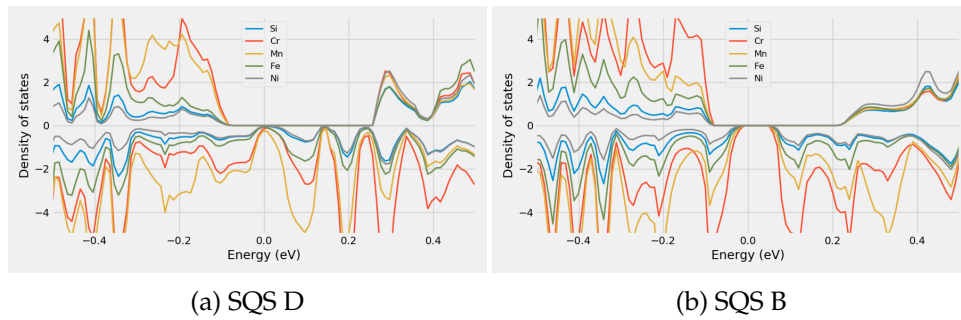


Figure 7.7: Projected density of states of SQS D and B around E_F

Comparing the PDOS of half-metallic SQS D (figure 7.7 a) to the configuration with the largest E_G^{dw} SQS B (figure 7.7 b), we find distinctly a large number of Mn states in SQS D around E_F most noticeably in spin down, but also in spin up. The PDOSs of the other 3 SQSs is included in appendix ..

7.2.3 The band gap with SCAN and HSE06

As expressed previously, in this work we invoke 3 level of depths GGA (PBE), meta-GGA (SCAN) and hybrid functional (HSE06) to determine the band gap. The outcome of these 3 functionals are showcased in table 7.4.

SQS	XC-functional	E_G^{up} (eV)	E_G^{dw} (eV)	E_G^{tot} (eV)
A	PBE	0.0815	0.0521	0.0281
	SCAN	0	0	0
	HSE06	0.7084	0.0261	0.0261
B	PBE	0.2932	0.0523	0.0523
	SCAN	0.1470	0.0890	0.0890
	HSE06	0.2855	0.1819	0.1819
C	PBE	0.2355	0.0343	0.0343
	SCAN	0.0690	0.1124	0.1124
	HSE06	0.1744	0.0328	0.0196
D	PBE	0.3386	0	0
	SCAN	0	0.1086	0
	HSE06	0.3780	0	0
E	PBE	0.3078	0.0495	0.0495
	SCAN	0.1540	0.1112	0.1048
	HSE06	0.5476	0.0133	0.0133

Table 7.4: Band gap calculated with PBE, SCAN and HSE06 XC-functionals of (CrFeMnNi)Si₂ SQSs.

We will begin dissecting table 7.4 by comparing SCAN to PBE. The first distinction we make notice of is in SQS A. In this supercell calculations with the SCAN functional predicts a metallic compound, contrary to the the PBE band gap of 0.03 eV. Alike the band gap of SQS D discussed previously, the 0 band gap in this structure with SCAN is caused by defect states. Neglecting such states and evaluating the band gap from just completely filled and empty eigenstates yield $E_{G,\text{SCAN}}^{\text{up,eigen}}(0.99,0.01) = 0.0316$ eV and $E_{G,\text{SCAN}}^{\text{dw,eigen}}(0.99,0.01) = 0.0531$ eV, and a total band gap of 0.0316 eV. This value seems to agree better with the PBE band gap of this supercell, but we observe that E_G^{up} is larger in PBE. This is a recurrent patter with SCAN across all five SQSs, where $E_{G,\text{SCAN}}^{\text{up}} < E_{G,\text{PBE}}^{\text{up}}$, and moreover $E_{G,\text{SCAN}}^{\text{dw}} > E_{G,\text{PBE}}^{\text{dw}}$. This can be seen in figure 7.8, where we plot the density of states of SQS E (a, b) and C (c, d). Note that the SCAN band gap in SQS C have the opposite spin polarization of PBE, this is also the case in SQS D as seen from table 7.4.

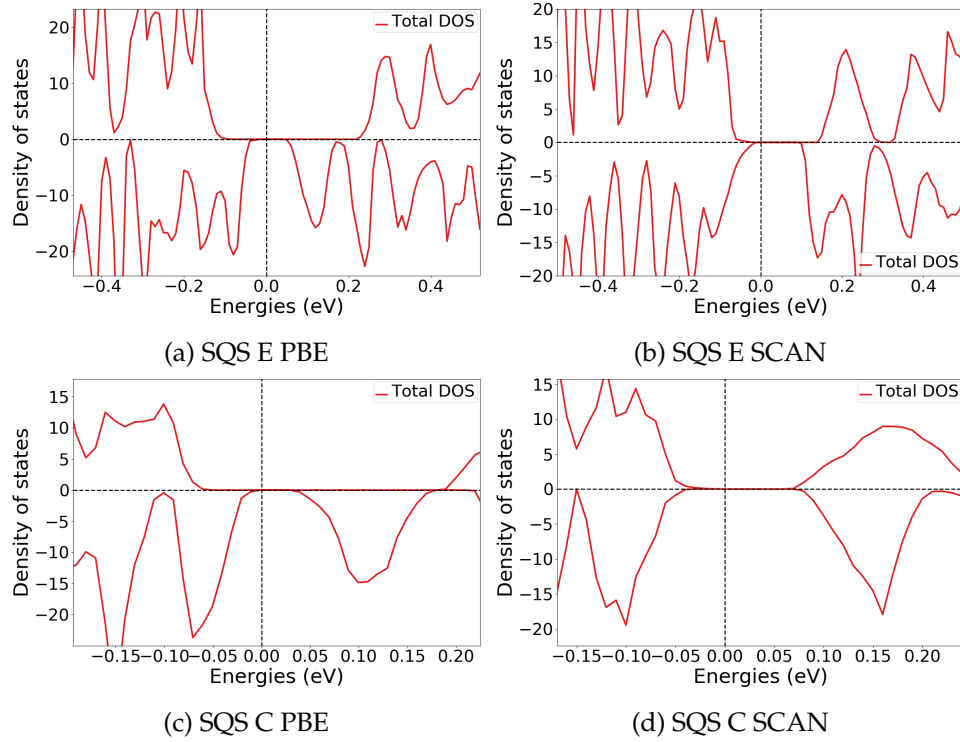


Figure 7.8: Density of states illustrating the band gaps from PBE and SCAN calculations for SQS E and D.

With the HSE06 functional we observe the opposite trend to SCAN in SQS A and E, where $E_{G, \text{HSE06}}^{\text{up}} > E_{G, \text{PBE}}^{\text{up}}$ and $E_{G, \text{HSE06}}^{\text{dw}} < E_{G, \text{PBE}}^{\text{dw}}$. But in other cases $E_{G, \text{HSE06}}^{\text{up}}$ is lesser (SQS C) or similar to PBE (SQS B and D). On the other hand $E_{G, \text{HSE06}}^{\text{dw}}$ is consistently smaller in all structures compared to PBE, with the exception of SQS B. In this structure the HSE06 functional predicts large band gaps in both spins, as seen from the density of states plotted in figure 7.8.

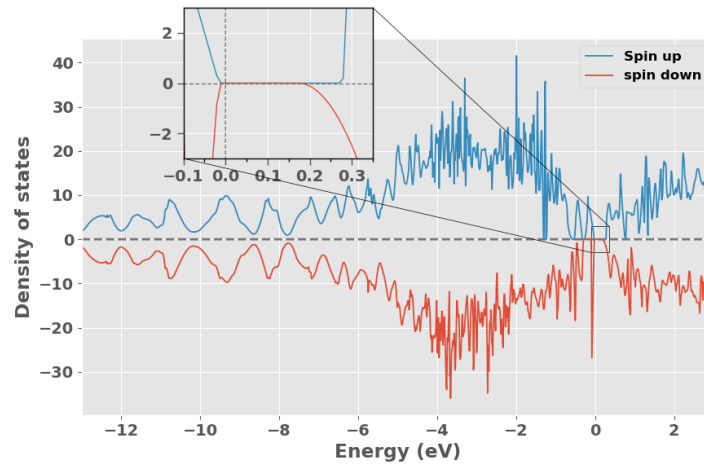


Figure 7.9: Density of states of SQS B with HSE06

As we discussed in section 5.1, hybrid functionals are much more computationally demanding compared to both meta-GGA and GGA functionals. In this project we experienced particular difficulty of converging calculations with HSE06 of the compositionally complex structures. To reduce the cost of the HSE06 functional we performed such calculations with a lower density of k-points, see section 6.1. The small amount of k-points could as discussed lead to numerical inaccuracies relating to the calculation of the Fermi surface in metallic structures. Furthermore the reduced mesh of k-points could result in artificially exaggerated band gaps from failing to encapsulate the exact minimum transition between the valence band and conduction band.

XC-functional	Transition (k-point)
PBE	(0.250,0.000,0.250) \rightarrow (0.000,0.000,0.000)
SCAN	(0.250,0.000,0.250) \rightarrow (0.000,0.333,0.000)
HSE06	(0.500,0.000,0.000) \rightarrow (0.000,0.000,0.000)

Table 7.5: Minimum gap between k-point in valence band and conduction band in SQS B from PBE, SCAN and HSE06

In table 7.5 we list the transition between the highest occupied k-state in the valence band and lowest unoccupied k-state in the conduction band for SQS B with PBE, SCAN and HSE06 respectively. We observe that all 3 functionals find different band gaps. A concerning factor is that the highest energy k-point in the valence band from PBE calculations (0.250, 0.000, 0.250) is not included in the HSE06 calculation with the narrow mesh of 2x2x2 k-points. Thus one may suspect that the HSE06 calculation overlook the minimum transition and hence return a enlarged band gap instead. This could be the case in $E_{G,A}^{up}$ and $E_{G,B}^{dw}$ where HSE06 predicts much larger values to PBE. However without an experimental baseline we can not conclude that this is the case. As in the other instances we find that HSE06 produce similar or lower band gaps compare to PBE despite of the smaller number of k-points.

As stated in section 6.2, we did not manage to converge hybrid calculations with the tetrahedron method, and overcame this problem by first calculating the charge density with Gaussian smearing and utilize the density to expedite TBC HSE06 calculations. The respective band gaps from these methods are displayed in table 7.6 for the five SQSs of the (CrFeMnNi)Si₂ system. Here we calculate the band gap from the eigenvalues at different cutoff occupancy *occ* to highlight the part of defect states. Gaussian smearing was tested with smearing width *sigma* equal to 0.05 eV and 0.005 eV.

SQS	Smearing (type) width (eV)	$E_G^{up,eigen}$ (0.5) (eV)	$E_G^{dw,eigen}$ (0.5) (eV)	$E_G^{up,eigen}$ (0.99) (eV)	$E_G^{dw,eigen}$ (0.01) (eV)	$E_G^{tot,eigen}$ (0.5) (eV)	$E_G^{tot,eigen}$ (0.99, 0.01) (eV)
A	Gaussian (0.05)	0.7837	0.1493	-	0.2984	0.1493	0.2984
	Gaussian (0.005)	0.2117	0.1013	-	-	0.1013	-
	TBC	0.7084	0.0261	-	-	0.0261	-
B	Gaussian (0.05)	0.2783	0.1702	0.2988	0.3136	0.1506	0.2979
	Gaussian (0.005)	0.2838	0.1823	-	-	0.1801	-
	TBC	0.2855	0.1819	-	-	0.1807	-
C	Gaussian (0.05)	0.1078	0.1066	0.2405	0.1839	0.0650	0.1839
	Gaussian (0.005)	0.1304	0.0222	-	-	0.0222	-
	TBC	0.1744	0.0328	-	-	0.0196	-
D	Gaussian (0.05)	0.3661	0.0592	-	0.1872	0.0592	0.1872
	Gaussian (0.005)	0.3736	0.0723	-	-	0.0723	-
	TBC	0.3780	0	-	0.2665	0	0.2637
E	Gaussian (0.05)	0.6653	0.1439	-	0.1675	0.1439	0.1675
	Gaussian (0.005)	0.5825	0.1211	-	-	0.1211	-
	TBC	0.5476	0.0133	-	-	0.0133	-

Table 7.6: Band gap from HSE06 calculations with Gaussian smearing and smearing width σ equal to 0.05 and 0.005, and the tetrahedron method (TBC). "-" means unchanged

From table 7.6 we observe that the presence and affect of defect states as discussed in section 7.2.1 is only present with Gaussian ($\sigma = 0.05eV$). Alike the previous cases, we find here finite band gaps despite of defect states. By comparing E_G^{up} and E_G^{dw} at $occ = 0.5$ and $occ = 0.01$, the defects appear to have a lesser role in spin up, as par SQS C the band gap in spin up is either consistent or only marginally different between the defect band gap and the hypothetical defect less band gap. E_G^{dw} on the other hand increase significantly by removing the defect states. The Gaussian smearing method is generally in better agreement with TBC at lower smearing width. But even in this case we find several dissimilarities. In A and E E_G^{dw} is larger with the Gaussian method, additionally E_G^{up} is much lower in SQS A. Furthermore the band gap of SQS D with HSE06 is with TBC in good agreement with the half-metallic compound found with PBE, meanwhile the Gaussian method ($\sigma = 0.005eV$) predicts a semiconductor with band gap equal to $0.07eV$. In this project we have based our choice of numerical smearing on the advice on the VASP manual that state that for accurate total energies and density of states in semiconductors one should opt for the tetrahedron method [5]. However since our system is comprised of metals as well as Si, we include the results from utilizing Gaussian smearing. There are of course many more factors that affect the accuracy and reliability of both methods, but these are outside the scope of this project.

The fact that all 3 functionals and five SQS in majority agree on the presence of a band gap is in itself an overwhelmingly positive result that allow us to state with high certainty that the potential high-entropy silicide (CrFeMnNi)Si₂ is in fact a semiconductor or possibly a half-metal based on the observed spin polarization and the utmost stable configuration. Regarding the 3 functionals applied in this project, we experience best cohesion between PBE and HSE06 that both agree on a spin up polarization of the band gap, while SCAN predicts more symmetric band gaps. This can also be seen from the magnetic moment, with PBE and HSE06 the final magnetic moment (per atom) is $0.083 \mu_B$ across all SQSs, with SCAN this is reduced to half the amount. In the nonmagnetic β -FeSi₂ structure we find better agreement between PBE and SCAN. Both correctly predict that the material is nonmagnetic, however compared to the experimental value of about $0.85 eV$ and the PBE band gap of $0.65 eV$, we get a smaller band gap of $0.61 eV$ with SCAN. Thus the SCAN functional does not necessarily result in increased accuracy over PBE even in the nonmagnetic material. To conclude this section on the band gap (CrFeMnNi)Si₂, when studying the band gap with DFT, particularly PBE is well known to underestimate the band gap of the real material as in FeSi₂. Therefore a band gap found with PBE would with high probability be replicated/increased in the real material. In the following sections and cases we will heavily emphasize the PBE functional to determine the band gap from both the fast and reliable use in addition to the point mentioned above. Furthermore from our experiences in this project in conjunction with the lack of literary support the SCAN function look to be ill-equipped for accurate band gaps. While the HSE06 functional is often to computationally expensive and

troublesome to converge for the structures in this project.

7.2.4 Pair distribution functions

The pair distribution functions of SQS D and B can be seen below in figure 7.10, the PDFs corresponding to SQS A, C, and E can be found in appendix .. . We include the PDFs of SQS D and B because as stated D is from the considerations made in this project the most stable atomic configuration and hence the most representative of the real random alloy. We analyze the PDF side by side to SQS B to investigate distinctions between the half-metallic configuration (D) and the semiconducting configuration (B).

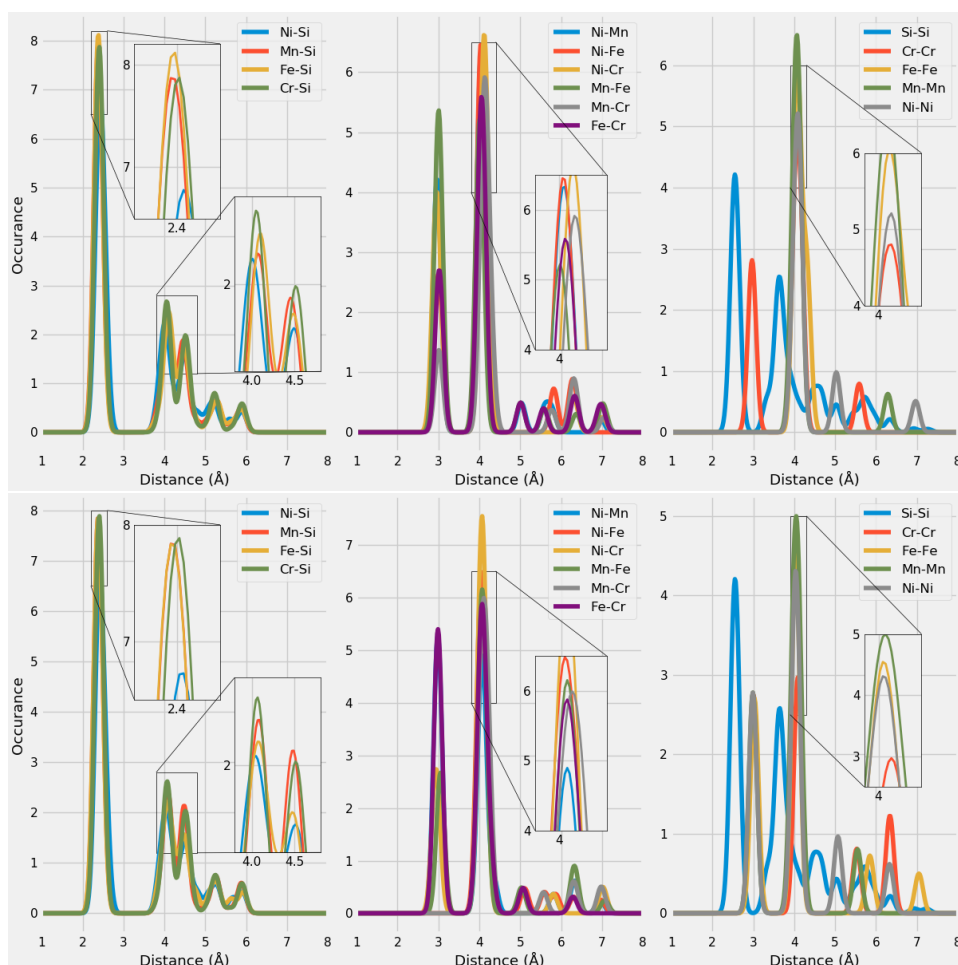


Figure 7.10: Pair distribution functions of SQS D (top) and B (bottom)

With the aid of the ICSD ([insert citation](#)), we can compare the PDFs in figure 7.10 to the expected PDFs based on a large number of experimental compounds. As our compound contains a total of 15 different bonds, comparing each one to the ICSD values would be an exhaustive process. According to the ICSD the preferred bond-length of TM-Si bonds is observed at two values, with the shorter length the most occurring. Specifically Fe-Si between 2.25-2.75 Å and 4-5 Å, Mn-Si at 2.25-2.75 Å and

3.5-5 Å, Ni-Si between 2.25-2.5 Å and 3.85-5 Å, and finally Cr-Si between 2.35-2.65 Å and 4-5 Å. Clearly, the PDFs of the SQSs are in good agreement with the listed values of TM-Si bonds. The relative occurrence of the bonds between SQS D and B are mostly consistent, other than marginally reduced Fe-Si occurrence at 2.4 Å in B.

In contrast, we observe several distinctions between TM-TM bonds in SQS D and B, for example Mn-Fe, Cr-Fe, and Ni-Mn bonds. This is simply a consequence of how the SQSs are generated, the silicon atoms are placed as before in the new supercells, but the TM elements are "randomly" distributed. Thus, it's reasonable that we would find the major differences between TM-TM bonds. Recalling that Mn had a distinct presence in spin down around E_F in SQS D, we observe that this structure compared to SQS B have a preference of Mn-Fe bonds at 3 Å and show larger occurrence of Mn-Mn bonds at 4 Å. However the differences between PDFs are difficult to relate to the observed properties. Firstly because of the sheer number of total bonds in the structures, and secondly considering the uniqueness of each SQS paired with the uncertainties regarding the stability.

7.2.5 SQS size

Above we have presented the results of a high-entropy silicide (CrFeMnNi)Si₂ investigated by 5 48-atom SQSs with a volume of 700 Å³. This intermediate size allowed us to apply different XC-functionals, and a broad study of different compositions which we will discuss in the next section. However the application of the SQS method to HEAs is not necessarily straightforward as we discussed in section 4.3. The most pressing concern is the size of the SQS model and if it's sufficient enough to correctly model the disordered multi-component structure. In this section we will evaluate this factor by studying the difference between the 48 atom SQSs discussed above to that of 96 and 192-atom SQSs with volume 1200 Å³ and 2400 Å³ respectively. The computational cost of the 3 sizes are included below in figure 7.11 in terms of the number of CPU hours.

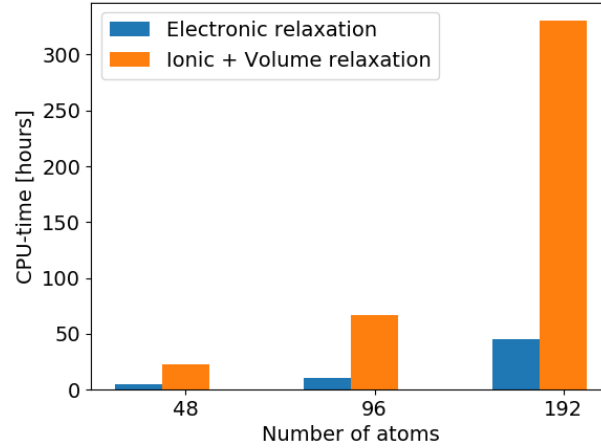


Figure 7.11: CPU time of 48, 96 and 192-atom SQSs of (CrFeMnNi)Si₂

Alike the 48-atom model, the 96 and 192-atom SQS were tested by 5 unique configurations. In table 7.7 we report the mean and standard deviation from the set of configurations for all three sizes, with respect to the total energy per atom and final magnetic moment per atom, in addition to the formation energy of the mean total energy.

SQS size	Toten (eV)		Mag (μ_B)		E_{FPA} (eV)
	mean	std	mean	std	mean
48 atoms	- 6.6105	..	0.0833	0.0000	-0.292
96 atoms	- 6.6092	0.0021	0.0708	0.0114	-0.292
192 atoms	- 6.6123	0.0022	0.0761	0.0171	-0.295

Table 7.7: Total energy, magnetic moment and formation energy of 48, 96 and 192 atom SQSs of (CrFeMnNi)Si₂

As seen from table 7.7 the total energy, magnetism and corresponding formation energy show very minimal variation between all three sizes, thus the 48-atom model is well converged. On the other hand we observe that the larger models contain larger deviation between configurations, this can be expected given the total number of atoms that can vary between configurations. The band gap corresponding to SQSs of each size are listed in table 7.8. First and foremost the band gap is evident in all three and exhibits analogous spin polarization, however the band gap appears to be less frequent and smaller in the larger structures.

SQS size	SQS	$E_G^{up,eigen}(0.5)$ (eV)	$E_G^{dw,eigen}(0.5)$ (eV)	$E_G^{tot,eigen}(0.5)$ (eV)
48 atoms	A	0.0815	0.0521	0.0281
	B	0.2932	0.0523	0.0523
	C	0.2355	0.0343	0.0343
	D	0.3386	0	0
	E	0.3078	0.0495	0.0495
96 atoms	A	0.1705	0.0442	0.0367
	B	0.1386	0.0270	0.0270
	C	0.1347	0.0363	0.0075
	D	0.0892	0.0398	0.0398
	E	0.1610	0	0
192 atoms	A	0.1197	0.0321	0.0321
	B	0.1444	0	0
	C	0.1867	0	0
	D	<i>0.0478</i>	<i>0.0339</i>	0
	E	<i>0.0131</i>	<i>0.0184</i>	<i>0.0131</i>

Table 7.8: Band gap of SQSs of 48, 96 and 192-atoms of (CrFeMnNi)Si₂. The names are arbitrary, ie A in 48 does not equal A in 96 or A in 192. The values listed in *cursive* indicate a defect band gap.

Equivalent to structure D in the 48 atom SQS we find that the 0 value in SQS E in the 48 atom model suffers from defect states, and $E_G^{dw,eigen}(0.90, 0.10) = 0.016$ eV. The same is true for SQS B and C (192), but require $occ = 0.999, 0.001$ to yield a finite band gap in spin down. The band gap in SQS D and E (192) on the other hand is finite at $occ = 0.5$ but can be enlarged from increasing occ , as we described for the Gaussian ($\sigma = 0.05$ eV) calculations previously. In SQS D (192-atoms) $E_G^{up,eigen}(0.99) = 0.075$ eV and $E_G^{dw,eigen}(0.01) = 0.05$ eV and similarly $E_G^{up,eigen}(0.99) = 0.05$ eV, and $E_G^{dw,eigen}(0.01) = 0.048$ eV in SQS E (192-atoms). In such cases where the eigenvalues inclusive of defect states return a finite band gap, the density of states does not. This is seen in figure 7.12 for SQS E in the 192-atom model that clearly have nonzero DOS at E_F in both spins.

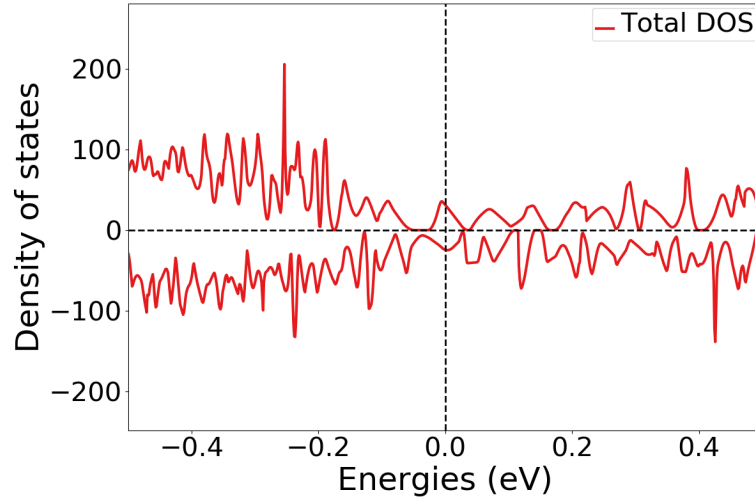


Figure 7.12: Density of states of SQS E 192 atom SQS.

One could wonder if the very narrow band gap from the eigenvalues of 0.01 eV is subject to numerical precision in the DOS. But on the grounds of the small value we calculated the DOS in this case by 20000 points over the energy range -12 eV to 12 eV which results in a resolution of about 8 points per 0.01 eV. In other words this should not be a factor of the DOS in figure 7.12.

Drawing any conclusion on the band gaps is difficult seeing as we find very different results within all 3 sizes. The utmost stable SQSs suggests that the band gap converge towards a small or possible non-existent band gap with increasing SQS size. On the other hand we also find evidence of large band gaps in the larger cells in less stable configurations. This goes back to section 3.3 where we mentioned that one particular difficulty of the SQS method is the large number of possible atomic configurations of one composition. We should note that for the sake of comparison, we conducted the calculations of the larger SQSs with identical computational parameters as the 48-atom models, this could affect the accuracy of the larger structures.

Looking at the pair distribution functions of the utmost stable SQS in each size (figure 7.13), we observe that short-range interactions is well represented and identical across all three models. The distinctions between preferences as discussed in section 7.2.4 is most likely a product of the uniqueness of the SQSs more so than the size. On the other hand the larger SQSs clearly provide a better description of large-range interactions, that is not nearly as present in the smaller supercell. But as seen from the minimal variation of the values in table 7.7 between the 3 models, in accordance with the fundamental philosophy of the SQS method that the functional properties are determined primarily from short-range interactions in the lattice. Thus, despite the fact that the larger SQSs offer improvement over the smaller SQSs, the gain is not justified by the cost. On the other hand, the SQS size looks to have more of an impact on the band gap of the material. But this could just as easily be a consequence of the sensitivity of the band

gap to the particular atomic configuration as seen in table 7.8.

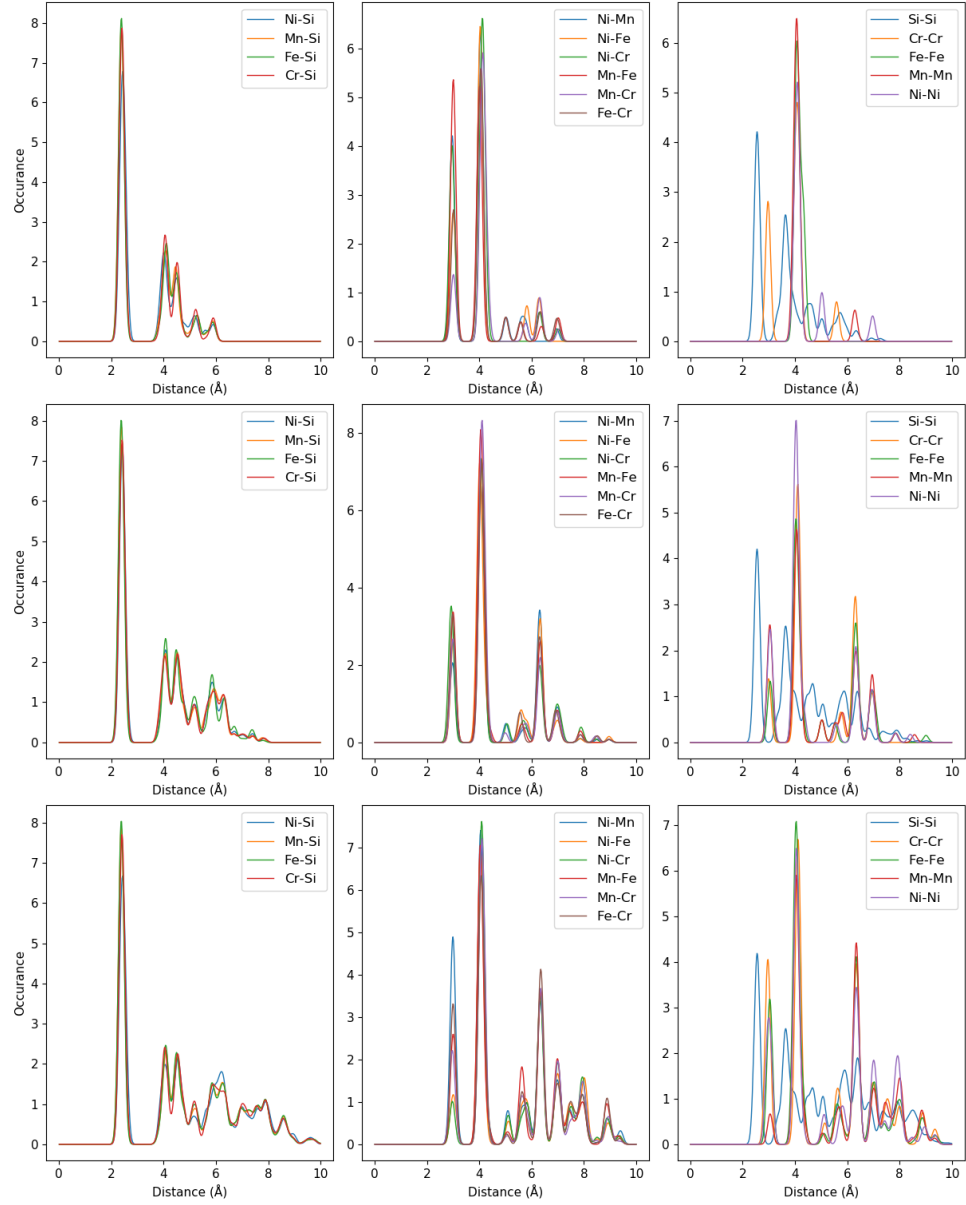


Figure 7.13: Pair distribution functions of SQS sizes (top) 48 atoms, (middle) 96 atoms, (bottom) 192 atoms

Chapter 8

Other compositions

Up until this point we have looked in detail at the high-entropy silicide (CrFeMnNi)Si₂ and associated SQSs. However these structures are just the center of a quaternary phase diagram consisting of the different possible distributions of elements. Thus there exists many other possible compositions related to the previously explored (CrFeMnNi)Si₂ high-entropy silicide. In the two following sections we will analyze some of the different possibilities, starting with a discussion on alloys based on the same elements but with different distributions. Thereafter we will look at alloys where chromium, manganese or nickel are replaced with cobalt or titanium.

8.1 Exploring the quaternary phase-diagram

In this section, we aim to expand our search of this diagram by generating SQSs of the 48 atom model slightly away from equimolar distribution of 3d elements. In table (bellow) we list the mean total energy and magnetic moment per atom with standard deviation and the enthalpy of formation of 4 compositions of the (CrFeMnNi)Si₂ alloy. Ideally they would differ only by one element, but the TDEP implementation insist in also reducing Nickel to stay consistent with the 48 atom supercell, therefore we include a composition with solely larger amounts of nickel as well.

Composition	Toten (eV)		Mag (μ_B)		E_{FPA} (eV)
	mean	std	mean	std	mean
Cr ₃ Fe ₃ Mn ₇ Ni ₃ Si ₃₂	- 6.6947	0.0040	0.1375	0.0186	-0.300
Cr ₅ Fe ₅ Mn ₃ Ni ₃ Si ₃₂	- 6.6705	0.0030	0.1127	0.0223	-0.286
Cr ₅ Fe ₃ Mn ₅ Ni ₃ Si ₃₂	- 6.6852	0.0041	0.1375	0.0456	-0.271
Cr ₃ Fe ₅ Mn ₅ Ni ₃ Si ₃₂	- 6.6801	0.0036	0.0937	0.0209	-0.315
Cr ₃ Fe ₃ Mn ₃ Ni ₇ Si ₃₂	- 6.3921	0.0078	0.0159	0.0101	-0.285

Table 8.1: Summary composition diagram

In table 8.1 we observe that moving away from the equimolar system generally result in lesser stable compositions, with the immense exception of compositions rich in nickel. Here we find that the formation energy is about twice the amount of the other compositions and additionally exceeds the equimolar system. The physical reason behind why nickel have such a large effect on the enthalpy of formation is beyond the scope of this study, but we do note that we have not found any indication of nickel stabilizing high-entropy alloys or silicides, but in terms of mathematics it's sensible that δH is larger from the low total energy of nickel (5.58eV) compared to for example Cr (9.51eV) or Mn (9.03).

Compared to the equimolar system, the magnetic moment of these compositions show a greater variation between SQSs, as indicated by the standard deviation. Typically the most stable SQS lie around the mean value of the set. The large magnetic moment of the manganese rich permutation and the low magnetic moment in the chromium poor permutation is very much in line with the observations made in the previous section. Recalling that in the magnetic moment in the equimolar composition was largely attributed to manganese and chromium atoms in the lattice. Thus increments to manganese or reduction of chromium would following impact the magnetic moment as seen. Following the composition $\text{Cr}_5\text{Fe}_3\text{Mn}_5\text{Ni}_3\text{Si}_{32}$ where the nonmagnetic elements are reduced and the magnetic elements are increased, the final magnetic moment is among the highest of the bunch equally magnetic.

In table 8.2 we list the respective band gaps of the different compositions calculated with the PBE functional. Only the GGA functional was applied in this case because the motivation is primarily to compare the results to the parent equimolar composition and thus including 3 times as many results to calculate and analyze unnecessarily complicate the process. Thus we base this comparison between the PBE results of the new compositions to the PBE band gaps of the equimolar compound. In these compositions we find strong indication of a half-metal with less frequent SQSs with a band gap in the spin down channel than the equimolar compound. In the spin up channel on the other hand several compositions show very similar values to the equimolar composition. Between the different compositions particularly those rich in manganese provide very encouraging results and compositions poor in Mn less so. In terms of the stability we a very encouraging results of both the $\text{Cr}_3\text{Fe}_3\text{Mn}_7\text{Ni}_3\text{Si}_{32}$ and $\text{Cr}_3\text{Fe}_5\text{Mn}_5\text{Ni}_3\text{Si}_{32}$ compositions, where the most promising properties is attributed to the utmost stable configurations. in $\text{Cr}_3\text{Fe}_5\text{Mn}_5\text{Ni}_3\text{Si}_{32}$ the most stable SQS (D) is a semiconductor with a band gap around 0.1 eV .

Composition	SQS	$E_G^{\text{up, eigen}}(0.5)$ (eV)	$E_G^{\text{dw, eigen}}(0.5)$ (eV)	$E_G^{\text{tot, eigen}}(0.5, 0.5)$ (eV)
$\text{Cr}_3\text{Fe}_3\text{Mn}_7\text{Ni}_3\text{Si}_{32}$	A	0.3390	0	0
	B	0.4745	0	0
	C	0.1342	0	0
	D	0.1950	0.0063	0.0063
	E	0.4211	0	0
$\text{Cr}_5\text{Fe}_5\text{Mn}_3\text{Ni}_3\text{Si}_{32}$	A	<i>0.003</i>	0	0
	C	<i>0.21</i>	0	0
	D	0.0674	0.0413	0.0372
	E	<i>0.362</i>	0	0
$\text{Cr}_5\text{Fe}_3\text{Mn}_5\text{Ni}_3\text{Si}_{32}$	A	0.2082	0	0
	B	0.4053	0	0
	C	0.4659	0	0
	D	0.0843	0.0121	0.0121
	E	0.3008	0	0
$\text{Cr}_3\text{Fe}_5\text{Mn}_5\text{Ni}_3\text{Si}_{32}$	A	0.3922	0	0
	C	0.1285	0	0
	D	0.2595	0.1004	0.1004
	E	0.3591	0.1003	0.0848
$\text{Cr}_3\text{Fe}_3\text{Mn}_3\text{Ni}_7\text{Si}_{32}$	A	0	0	0
	B	0	0	0
	C	0	0	0
	D	0	0	0
	E	<i>0.04</i>	0	0

Table 8.2: Band gaps of various compositions of $(\text{CrFeMnNi})\text{Si}_2$. Most stable SQS of a set is highlighted in bold text, defect band gap are listed in cursive. Some SQSs were excluded from the table due to unsuccessful calculations.

Below in figure 8.1 we plot the projected density of states around E_F of the first four compositions of table 8.2. Note that away from the Fermi energy the projected density of states is analogous to the parent equimolar composition. The below figures is based on the most stable SQS in each permutation, as will the analysis. Hence the features of these figures can be subject to the uniqueness of that particular SQS rather than a distinct feature of the exact composition, but as stated previously the most stable configuration provide the most likely properties of the composition within the scope of this project.

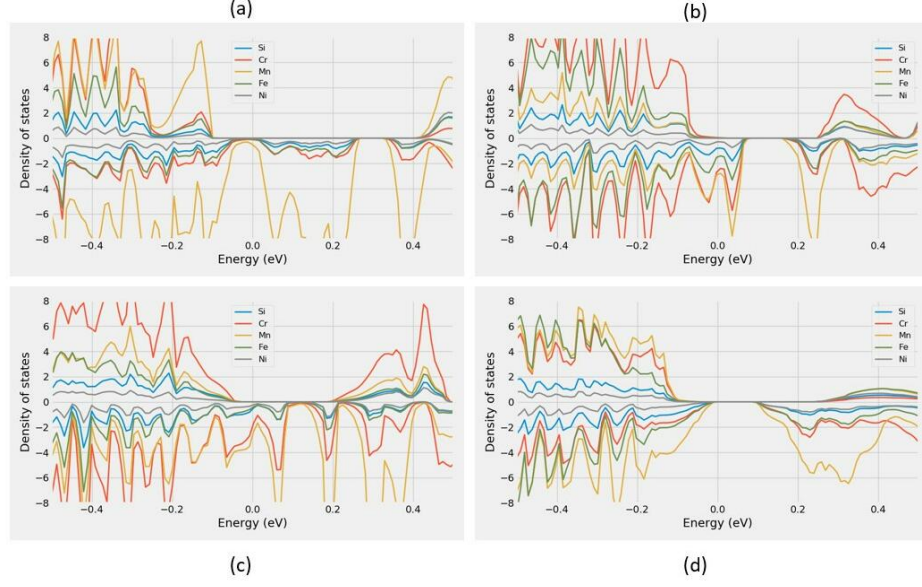


Figure 8.1: Projected density of states of (a) $\text{Cr}_3\text{Fe}_3\text{Mn}_7\text{Ni}_3\text{Si}_{32}$ (SQS B), (b) $\text{Cr}_5\text{Fe}_5\text{Mn}_3\text{Ni}_3\text{Si}_{32}$ (SQS C), (c) $\text{Cr}_5\text{Fe}_3\text{Mn}_5\text{Ni}_3\text{Si}_{32}$ (SQS A), (d) $\text{Cr}_3\text{Fe}_5\text{Mn}_5\text{Ni}_3\text{Si}_{32}$ (SQS D)

With that said, the plotted PDOSs in figure 7.1 is in good agreement with the listed values in table 7.2. $\text{Cr}_3\text{Fe}_3\text{Mn}_7\text{Ni}_3\text{Si}_{32}$ (7.1 a) and $\text{Cr}_5\text{Fe}_3\text{Mn}_5\text{Ni}_3\text{Si}_{32}$ (7.1 c) both indicate a sizable spin up band gap, further figure (7.1 d) point to a total band gap around 0.1 eV for SQS D of $\text{Cr}_3\text{Fe}_5\text{Mn}_5\text{Ni}_3\text{Si}_{32}$. On the other hand we find dissimilarity between the density of $\text{Cr}_5\text{Fe}_5\text{Mn}_3\text{Ni}_3\text{Si}_{32}$ SQS C and the eigenvalue band gap listed in table 7.2. In figure 7.1 d we find a range of forbidden energies slightly above the Fermi energy, and very small values in spin up at the Fermi energy. Similar to what we experienced in the 192 atom SQS in section 7.4, the eigenvalues report a finite band despite of defect states. Therefore the density of states is not completely zero at E_F .

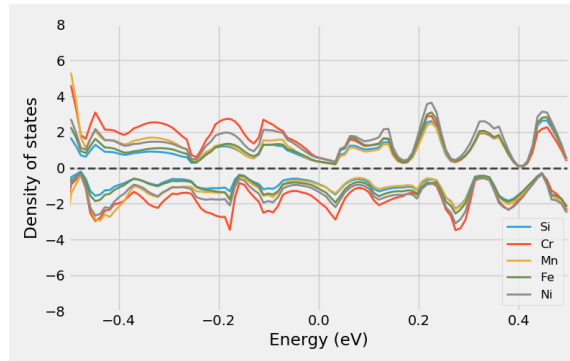


Figure 8.2: Projected density of states of $\text{Cr}_3\text{Fe}_3\text{Mn}_3\text{Ni}_7\text{Si}_{32}$ around E_F

In figure 8.6 we saw that electrons from manganese atoms in particular was a key contributor as to why the spin down channel of $(\text{CrFeMnNi})\text{Si}_2$

was metallic in the stable supercell D. This is also largely the case in the permutations shown above in figure 8.12. The proportion of manganese atoms in the alloy seems to offer a very positive effect on the band gap in spin up, but is often detrimental to spin down. This is seen in figure 8.12 (a) and (c) for $\text{Cr}_3\text{Fe}_3\text{Mn}_7\text{Ni}_3\text{Si}_{32}$ and $\text{Cr}_5\text{Fe}_3\text{Mn}_5\text{Ni}_3\text{Si}_{32}$ respectively, that both contain increased amounts of manganese. By reducing the number of Mn as in (b) we still find that the Mn electrons plague the states at E_F in spin down. In analog we see from (b) and (c) that also Cr negatively impacts to the band gap especially in spin up. The sole permutation with clear evidence of a spin down gap is from the chromium poor permutation plotted in (d). Also in this structure we see that the effects of Mn around E_F is dampened in comparison to the other permutations, despite containing relatively increased amounts of Mn to the eqvimolar alloy.

An important property of these results is that because each composition alters simultaneous elements, interpreting and relating the results to a particular alteration is challenging. For example, is the result of the $\text{Cr}_5\text{Fe}_3\text{Mn}_5\text{Ni}_3\text{Si}_{32}$ permutation a consequence of less Fe or increments to both Cr and Mn? Furthermore is the large band gap in spin up of $\text{Cr}_3\text{Fe}_3\text{Mn}_7\text{Ni}_3\text{Si}_{32}$ a product of increasing manganese or reducing the other elements. From the comparatively large gaps in spin up of $\text{Cr}_3\text{Fe}_3\text{Mn}_7\text{Ni}_3\text{Si}_{32}$ and $\text{Cr}_3\text{Fe}_5\text{Mn}_5\text{Ni}_3\text{Si}_{32}$ and the more present Cr states in spin up in the Cr rich permutations we here conclude that the band gap is related to lessening of chromium, more so than other effects. However we see from both $\text{Cr}_5\text{Fe}_5\text{Mn}_4\text{Ni}_3\text{Si}_{32}$ and $\text{Cr}_3\text{Fe}_3\text{Mn}_3\text{Ni}_7\text{Si}_{32}$ (figure 8.2) in addition to the manganese rich composition that Mn plays a vital role on the band gap of these structures. It's clear that the $\text{Cr}_3\text{Fe}_5\text{Mn}_5\text{Ni}_3\text{Si}_{32}$ alloy manage to strike a balance between 3d elements that results in a specific interplay and correspondingly very promising properties. In addition we see from the enthalpy of formation that the compositions poor in chromium are more stable than the chromium rich compositions.

8.2 High entropy silicides with cobalt and titanium

In similar fashion to the previous sections, we here begin by presenting the mean and standard deviation of the total energy and magnetization of a set of SQSs corresponding to different high-entropy silicides of the FeSi_2 unit cell. The compositions we have tested are deliberate combinations intended to investigate both the impact of manganese by replacing the element with Co or Ti, and concepts related to HEA theory such as the atomic size effect. Furthermore Co is a very common element in many stable HEA, as seen in section 2.2, thus we include 3 compositions with Co to study the impact on stability and the functional properties. The results of the aforementioned alloys can be seen below in table 9.1, note that all compounds contain a total of 48 atoms as before.

Composition	Toten (eV)		Mag (μ_B)		E_{FPA} (eV)
	mean	std	mean	std	mean
$\text{Cr}_4\text{Fe}_4\text{Co}_4\text{Ni}_4\text{Si}_{32}$	-6.4655	0.0056	0.0083	0.0155	-0.308
$\text{Co}_4\text{Fe}_4\text{Mn}_4\text{Ni}_4\text{Si}_{32}$	-6.4731	0.0046	0.0000	0.0000	-0.355
$\text{Cr}_4\text{Fe}_4\text{Ti}_4\text{Ni}_4\text{Si}_{32}$	-6.4217	0.0087	0.0305	0.0293	-0.209
$\text{Cr}_4\text{Fe}_4\text{Mn}_4\text{Ti}_4\text{Si}_{32}$	-6.6994	0.0071	0.1142	0.0641	-0.199
$\text{Cr}_4\text{Fe}_4\text{Mn}_4\text{Co}_4\text{Si}_{32}$	-6.7687	0.0034	0.1331	0.0326	-0.323

Table 8.3: Overview new compositions

From table 9.1 we see that the stability of the relative compositions vary greatly. By introducing cobalt to the alloys, particularly at the cost of chromium result in a large positive effect on the stability, contrary replacing either manganese or nickel with titanium significantly lowers the stability. A physical interpretation of the relative stability is difficult from the overall shallow emphasis and analysis in this project, but we do note that the two most stable alloys consist of the most chemically similar elements in terms of properties such as electronegativity and atomic size. Following the least stable alloys according to our study is comprised of the most chemically dissimilar elements. This is in good agreement with our discussion in section 2.2 regarding phase formation of high-entropy alloys.

In table 9.1 we have listed the mean magnetic moment of the compositions, in line with previous results in this project the magnetization is very dependent on chromium and manganese. This is seen by the overall lowest magnetic moments in the two compositions without these elements, and reversely the highest magnetic moments is found for compositions with both Cr and Mn. Comparing the magnetic moment of $(\text{CrFeCoNi})\text{Si}_2$ and $(\text{CoFeMnNi})\text{Si}_2$ it seems in our study that chromium is most responsible for the magnetic moment in these alloys. Furthermore we find that substituting Ni with both Ti and Co result in more magnetic compounds. These are truly surprising results, one would expect that the magnetic moments would be larger in the ferromagnetic elements Ni, Fe and Co than Cr, Mn and Ti. This could go back to our simplistic and superficial study of the magnetic properties in this project, additionally the PBE functional as we covered in section .. have shown limitations for 3d elements and particularly Ni. Thus this could be a factor affecting our results. Another factor is that we here based our comparison on the mean values between 5 SQSs. As we have experienced throughout this project the uniqueness of the SQSs can be troublesome to handle, and our best guess is to study the most stable super-cell. Below in table 9.2 we list the magnetic moments of the most stable SQSs. Here we find several dissimilarities to the mean value such as the $\text{Cr}_4\text{Fe}_4\text{Co}_4\text{Ni}_4\text{Si}_{32}$ being nonmagnetic in the most stable supercell. Thus based on the utmost stable configurations we can state that replacing either Cr or Mn (with Co) removes the magnetic moment in the alloy. Furthermore we find from these supercells that the magnetic moment is reduced

by replacing Ni with Ti, and increased from Co. These results are in much better accordance with previous knowledge of ferromagnetic elements and their interplay in high-entropy alloys.

Composition	Magnetic moment (μ_B)
$\text{Cr}_4\text{Fe}_4\text{Co}_4\text{Ni}_4\text{Si}_{32}$	0
$\text{Co}_4\text{Fe}_4\text{Mn}_4\text{Ni}_4\text{Si}_{32}$	0
$\text{Cr}_4\text{Fe}_4\text{Ti}_4\text{Ni}_4\text{Si}_{32}$	0,0653
$\text{Cr}_4\text{Fe}_4\text{Mn}_4\text{Ti}_4\text{Si}_{32}$	0,0785
$\text{Cr}_4\text{Fe}_4\text{Mn}_4\text{Co}_4\text{Si}_{32}$	0,1666

Table 8.4: Final magnetic moment of the most stable supercell of each composition.

In regards to the band gap of these compositions, we find most to be metals. The band gap of the most stable SQS of each composition is listed in table 4.3, where we calculate the band gap from the eigenvalues at different occupancy cutoffs. As before the 0 band-gap is caused by defect states in the band gap. By increasing the criteria, in other words only consider states with occupancy above a certain threshold, the band gap become finite at $occ = 0.1$ and converge to around 0.02 – 0.06 eV depending on composition, when only considering full/empty states.

Composition	occ	$E_G^{\text{up, eigen}}$ (eV)	$E_G^{\text{dw, eigen}}$ (eV)	$E_G^{\text{tot, eigen}}$ (eV)
CrFeCoNiSi_2	0.5	0	0	0
	0.1	0.00095	0.0399	0.00095
	0.01	0.063	0.063	0.063
CrFeTiNiSi_2	0.5	0.0067	0	0
	0.1	0.061	0.0087	0.0087
	0.01	0.061	0.037	0.037
CoFeMnNiSi_2	0.5	0	0	0
	0.1	0.0037	0.0037	0.0037
	0.01	0.0268	0.0268	0.0268
CrFeMnTiSi_2	0.5	0	0	0
	0.1	0.021	0.00049	0
	0.01	0.03	0.03	0.022
CrFeMnCoSi_2	0.5	0.461	0	0
	0.1	0.607	0.0218	0.0218
	0.01	0.607	0.0245	0.0245

Table 8.5: Band gaps of the most stable SQS of β -FeSi₂ high-entropy silicide compositions as a function of occupancy in the eigenvalues.

In the CrFeMnCoSi_2 composition we observe a band gap of around 0.5 eV in the spin up channel, contrary to the metallic or very narrow band gaps in the other compositions. But also in this case we find that the eigenvalues contain defect states, by the fact that the band gap can be enlarged at lower values of occ . As we have covered for other examples in this project, this results in a metallic density of states with a small number of states at the Fermi energy. This can be seen from the projected density of states in figure 8.3. This is a contradicting result to the eigenvalues, as per the definition, a band gap is defined as a range of energies around E_F with no states. On the other hand, this result could rather be related to numerical factors affecting the accuracy of the density of states, such as a low resolution or number of k-points considering the very marginal difference separating the density of states from a metal to a half-metal.

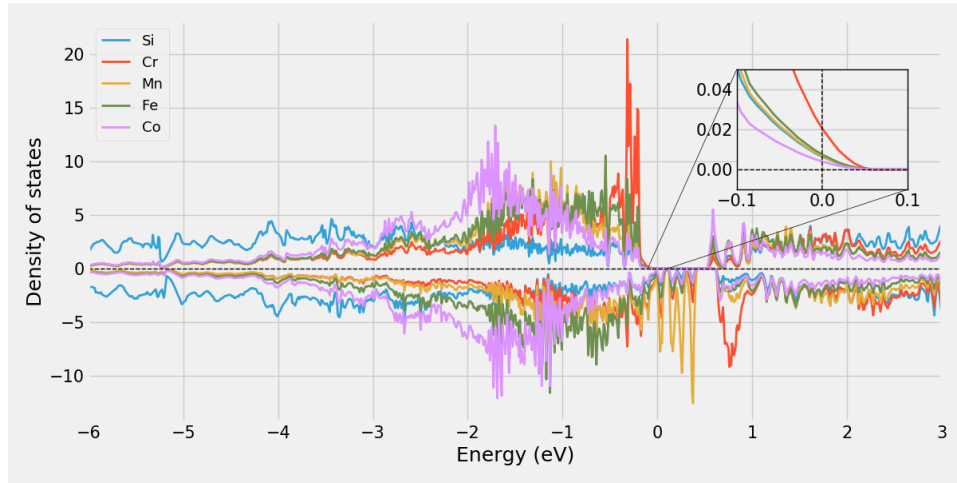


Figure 8.3: Projected density of states of $(\text{CrFeMnCo})\text{Si}_2$.

The concept of defect states remain as the unsolved biproduct of this project, that we have seen is clearly related to a metallic structure, but is less prominent in the alloys. However considering the scope and allocated time/resources of this project we have not been able to investigate this concept further and found minimal literature to base our results and discussion on. Thus we are unable to provide a conclusion on firstly the significance and physical interpretation of it, and secondly why they appear in some compositions/structures but not others but report that it's less apparent in the $(\text{CrFeMnNi})\text{Si}_2$ system. One possible method of analyzing it could have been to study more in depth the pair distribution functions and compare between all compositions, but given the uniqueness of the SQSs and number of bonds in each structure this falls outside the scope of this project. We report the related PDF's of each composition in appendix .. but do not discuss them. The projected density of states of each composition is found in appendix ..

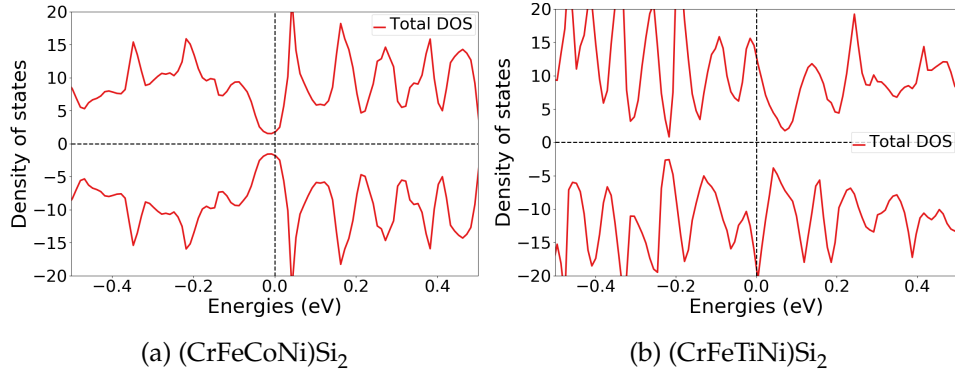


Figure 8.4: Density of states of a) (CrFeCoNi)Si₂ and b) (CrFeTiNi)Si₂.

Contrary to the above case, inserting Co in the place of manganese clearly result in a metallic structure, as seen in the density of states in figure 9.2 a. Replacing Mn with Ti instead we recall from table 9.3 a a very small defect band gap in spin up, however from figure 9.2b we observe that E_G^{dos} is equal to zero, thus again $E_G^{dos} \neq E_G^{eigen}$. Comparing the density of states of (CrFeCoNi)Si₂ and (CrFeTiNi)Si₂ the latter is magnetic and the former nonmagnetic, as we discussed previously.

Above we have looked at the band gap of the most stable SQS of each composition, but as we have experienced in other cases in this project, the properties can vary between SQSs of the same composition. In both CrFeCoNiSi₂ and CrFeMnTiSi₂ we found only metallic supercells with the exception of one SQS in the latter with a very small defect band gap in spin up. Similarly small defect band gaps was observed in two SQSs of CrFeTiNiSi₂ and the rest as metals. In CrFeMnCoSi₂ we found a large defect band gap in spin up in the most stable configuration, here we find similar band gaps in two other SQSs as well. The most interesting case was found in CoFeMnNiSi₂ where we observed small total band gaps without defect states in two SQSs, these are seen in figure 9.3. In agreement with the nonmagnetic character of this composition, the DOS is symmetric with respect to spin.

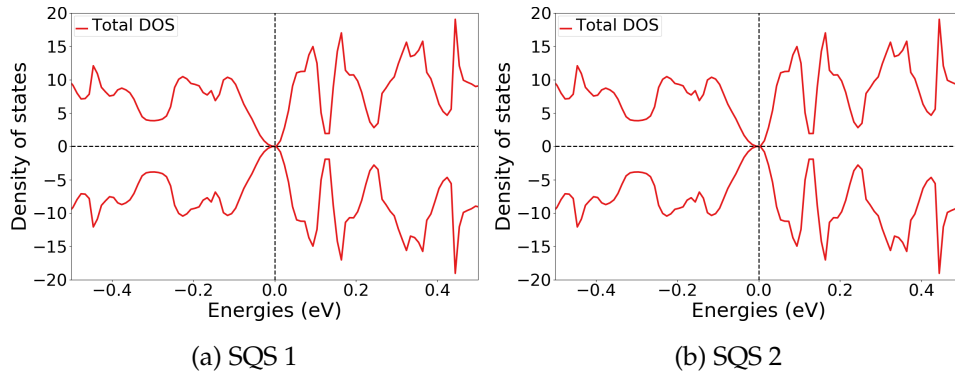


Figure 8.5: Density of states of two lesser stable SQSs of (CoFeMnNi)Si₂.

In this example, and also throughout this project we have experienced

scenarios where the most stable SQS represents the set of supercells well, and in other instances where the properties change from supercell to supercell. Because of the limited efforts on the magnetism and corresponding stability of the alloys in this project, we chose to include and discuss all 5 SQSs in several cases. This goes back to the topics discussed previously in which one might expect the real material to be comprised of domains of local ordering equal to each one of the SQSs and other possible configuration by a probability based on the relative stability. Furthermore we have reservations about the SQS approach in general to produce an accurate depiction of the true disordered structure, particularly at the relative small size. As we experienced in section .., noteworthy the band gap and PDFs showed distinctions between cells, an additional point to this is that the SQS method have prior limitations of compositions with large deviation from the equiatomic composition, compared to methods such as the CPA for instance.

Now that we in this study have quite qualitatively determined the existence of a band gap in a potential high-entropy silicides, and according to our calculations in the $(\text{CrFeMnNi})\text{Si}_2$ composition based on the cmce crystal structure. In future work we would first and foremost do a more comprehensive configuration of the magnetic moments to qualitatively determine the ground state energy and compare the relative stability between a broader number of crystal structures. Going back to section 4.3, one of the key drawbacks of the DFT is that we only find local minima, thus from this project we have no knowledge of this particular composition stabilize in the structure tested in this project or another one. On this topic, recent findings have supported high-entropy silicides stabilizing in less symmetric structures such as orthorhombic and hexagonal **Cite this and that** as opposed to initial studies indicating that HEAs are primarily found in simple cubic lattices. But this should be tested nevertheless. With a more precise conclusion on both geometric and magnetic factors of the material, we could have performed a deeper analysis of the band gap and put more effort into converging calculations without uncertainties of band-gap specialized functionals such as HSE06 and MBJ, and to a greater extent investigated the defect states in the eigenvalues, and relate this qualitatively to a physical or numerical factor.

Following studies on the ground state geometry and energy, the composition should be exposed for finite temperatures to evaluate the magnetism and transition temperatures, and entropic contributions to the stability through Gibbs law, in addition to a number of other considerations. Nevertheless we have succeeded atleast within the scope of this project, in our task of locating high-entropy alloys/silicides with a band gap. Furthermore the magnitude of the band gap in many instances (between 0.01 - 0.1 eV), if we assume that the PBE GGA underestimate the band gap between 30% – 50% would make for promising candidate thermoelectric materials. However to qualitatively state the promise of these compositions as thermoelectrics one would have to investigate properties such as the Seebeck coefficient in addition to the electrical and thermal conductivity. But based on the findings of similar materials to the one in

this project, such as .. that found lowered thermal conductivity in .. and ,.. in this and that, the possibility of an effective thermoelectric material is not beyond hope. In addition the strong magnetism and spin polarization of the band gap displayed in this material (according to our narrow study) makes it a promising candidate for spintronics application.

Do the magnetic discussion here or some other place where I summarize the magnetic findings and relate to other studies. Discuss why Fe and Ni for instance is low and Mn and Cr high. We find this to be somewhat of a strange result, in agreement with prior conceptions of the magnetism in various 3d transition metals we find from individual calculations of the base elements in their stable configuration under exact conditions as the SQSs, that Fe display the most pronounced magnetic moment, followed by nickel, while both manganese and Cr are nonmagnetic. Source for Mn

Part IV

Conclusion

Write conclusion here

Bibliography

- [1] S. J. Clark et al. 'Structure and electronic properties of FeSi_2 '. In: *Phys. Rev. B* 58 (16 Oct. 1998), pp. 10389–10393. DOI: 10.1103/PhysRevB.58.10389. URL: <https://link.aps.org/doi/10.1103/PhysRevB.58.10389>.
- [2] Voicu Popescu and Alex Zunger. 'Effective Band Structure of Random Alloys'. In: *Phys. Rev. Lett.* 104 (23 June 2010), p. 236403. DOI: 10.1103/PhysRevLett.104.236403. URL: <https://link.aps.org/doi/10.1103/PhysRevLett.104.236403>.
- [3] H Lange. 'Electronic properties of semiconducting silicides'. In: *physica status solidi (b)* 201.1 (1997), pp. 3–65.
- [4] R. Eppenga. 'Ab initio band-structure calculation of the semiconductor $\beta\text{-FeSi}_2$ '. In: *Journal of Applied Physics* 68.6 (1990), pp. 3027–3029. DOI: 10.1063/1.346415. eprint: <https://doi.org/10.1063/1.346415>. URL: <https://doi.org/10.1063/1.346415>.
- [5] *ISMEAR - Vaspwiki*. URL: <https://www.vasp.at/wiki/index.php/ISMEAR>.